JACS
JOURNAL OF THE AMERICAN CHEMICAL SOCIETY
pubs.acs.org/JACS
Article

Spin Polarization Enhanced Ethanol Selectivity in Electrocatalytic CO_2 Reduction on the Paramagnetic CuO Surface

Fujun Tao,[¶] Jianxin Wang,[¶] Jiayi Xu,[¶] Guangji Chen, Xudong Xiao, Mengyuan Li, Haozhe Zhang, Xinwei Zhou, Yuzi Liu, Owen S. Wostoupal, Zhenzhen Yang, Bing Shi, H. Christopher Fry, John E. Pearson, Haiming Li, Chong Zheng, Cong Liu,* Di-Jia Liu,* and Tao Xu*

Cite This: https://doi.org/10.1021/jacs.6c05085
Read Online

ABSTRACT: We report an electrochemical CO_2 reduction reaction catalyzed by a paramagnetic and conductive CuO/Cu interface with spins polarized by a moderate external magnetic field (MF) of ~800 gauss, achieving a ~30% increase in CO_2-to-C_{2+} Faradaic efficiency (FE) compared to that in the absence of the MF in a flow cell electrolyzer. At a current density of 400 mA/cm^2, the CO_2-to-C_{2+} FE reached 86.7 ± 2.7% with 47.9 ± 1.4% cathodic energy efficiency (EE) in contrast to the CO_2-to-C_{2+} FE of 67.6% with 36.4% of EE in the absence of MF. Notably, ethanol production exhibits a much higher response to the MF (~55.6% increase in FE) than ethylene (~6.4% increase in FE) at 400 mA/cm^2. In situ surface-enhanced Raman spectroscopy (SERS) captured magnetic-field-enhanced *CO coverage and ethanol-forming C_2 intermediates on CuO/Cu, providing direct spectroscopic evidence of spin-modulated pathway selection. Computational study suggests that the enhancement of ethanol selectivity is due to the reduced reaction kinetic barrier under MF, while the ethylene selectivity is less affected, mainly due to the insensitivity of the kinetic barriers under MF.

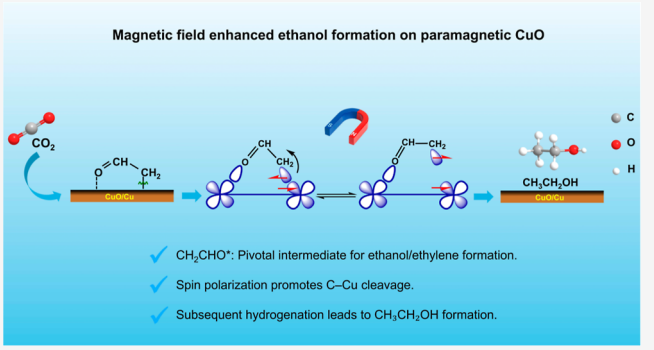

INTRODUCTION

The economic challenge of electrosynthesis of organic molecules via electrochemical CO_2 reduction reaction (CO_2RR) is mainly due to the electrical energy cost. The input electrical energy for CO_2RR is regulated by the potential difference between the cathode and anode. Besides lowering the voltage for reduced electrical power consumption, it is also crucial to direct the electric charge toward selective conversion of high-value products for better economic viability. Organic products containing high-energy chemical bonds, such as C−H and C−C or C═C bonds (C_{2+} products), generally have high economic values. At present, studies on improving the selectivity of producing C_{2+} compounds by CO_2RR have been focused on developing new electrocatalysts, electrolytes (e.g., ionic liquid) and operating parameters (e.g., pressure and temperature).[1−8] Given the electron-transfer nature of CO_2RR and the quantum mechanical wave nature of electrons, the effect of magnetic field (MF), which can influence the electronic orbitals and spin magnetic moments through unpaired electrons[9,10] in CO_2RR intermediates, has rarely been exploited.[11−13] The electron transfer from catalysts to receptors (e.g., CO_2, H^+, and intermediates) should depend on the orbital and/or spin symmetry at the receptor−catalysts interface. Therefore, MF could potentially modulate such interaction in controlling the reaction path, hence the current density toward one or more specific product conversion over others in CO_2RR. Previous studies on magnetic-field-assisted CO_2RR have reported enhancements of C_1 products under high current density,[14,15] while C_{2+} products were only modestly promoted under low current density conditions.[12] For instance, enhancement in C_1 products such as CO by magnetic-field-assisted CO_2RR was reported.[14] Another study observed modest promotion of C_{2+} products under low current density (~5 mA/cm^2) in H-cell setups.[12] However, achieving selective C_{2+} production under high current density meaningful for industrial applications remains a major challenge. Here, we demonstrate that an external magnetic field can markedly enhance C_{2+} formation under high current density up to 200 mA/cm^2. This effect arises from imparting a net spin to the CuO/Cu electrocatalyst, which acts as a "gripper" for the magnetic field to modulate the spin entropy-related exchange−correlation energy between the electrocatalysts and the

Received: March 10, 2026
Revised: April 24, 2026
Accepted: May 1, 2026

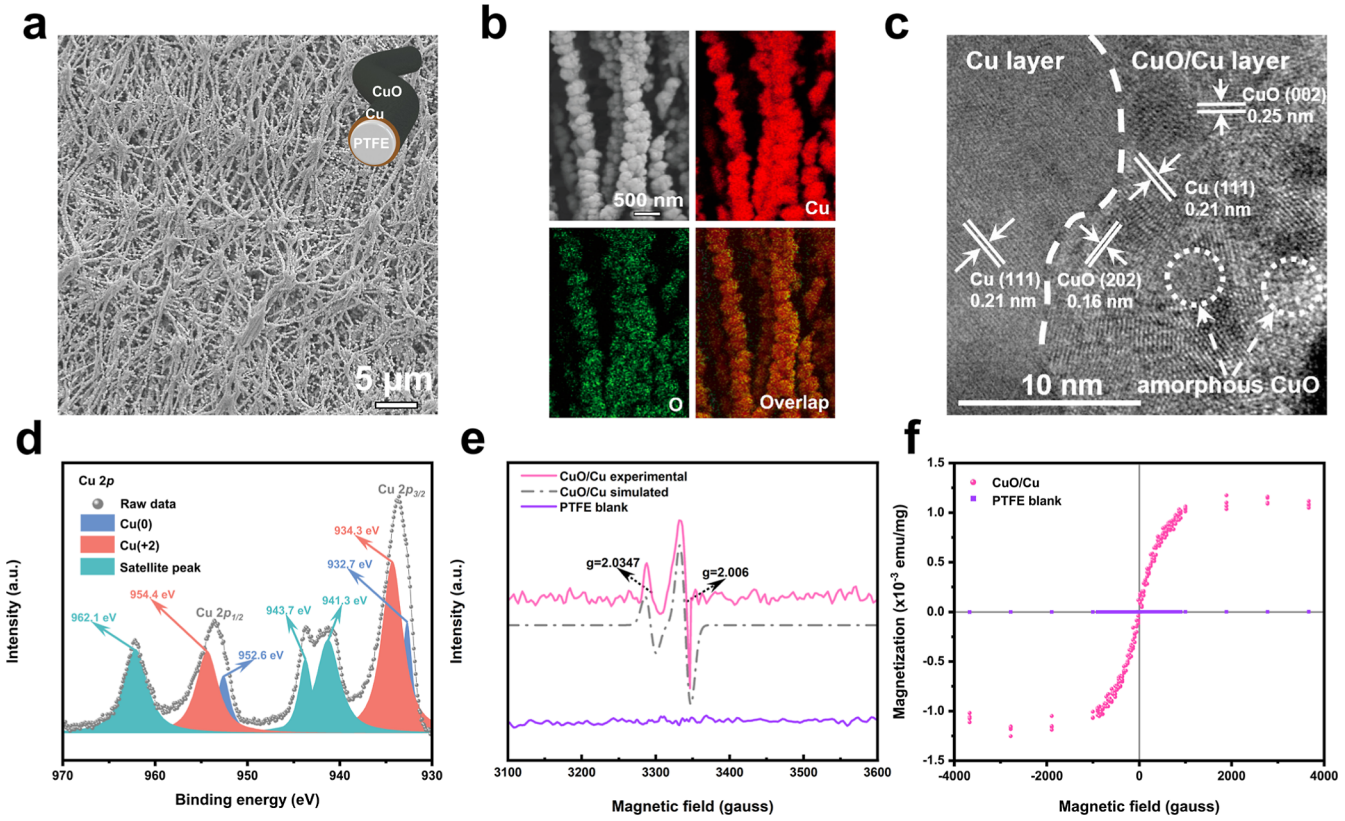

Figure 1. Structural and spectroscopic analyses of CuO/Cu on PTFE. (a) Low-magnification SEM image of CuO/Cu on PTFE. Inset: schematic cross-section of CuO/Cu on the PTFE nanofiber film. (b) EDX elemental mapping of Cu, O, and their overlap for the CuO/Cu catalyst on PTFE. (c) HRTEM at the catalyst interface between Cu and CuO. (d) High-resolution Cu 2*p* spectra of CuO/Cu on PTFE. (e) EPR spectra of PTFE background and CuO/Cu on PTFE. (f) Magnetization curves of PTFE background and CuO/Cu on PTFE.

adsorbed C_2 intermediates,[15] thereby altering the selectivity of CO_2RR.

Bulk copper metal is diamagnetic because the unpaired electrons ($4s^1$) form a sea of delocalized (itinerant) free conducting electrons (metallic bond) throughout the entire copper metal, losing their unpaired nature. In contrast, CuO is paramagnetic ascribed to the $[Ar]3d^94s^0$ electron configuration of the Cu^{2+} species in CuO, thus creating a relatively localized spin in its d orbitals. CuO is a p-type semiconductor with its conductivity originated from the electrons hopping through the Cu−O bonds (equivalent to hole transport along the opposite direction).[16] As discussed below, when polarized by an external MF, the magnetic moment of the localized d spins in Cu^{2+} is preferentially aligned along the field, which further affects the bond formation and cleavage of the C_2 intermediates on the CuO surface. We show that MF preferentially promotes the C−Cu bond cleavage of the C_2 intermediate on the CuO containing 3d spin, a key step toward enhanced ethanol formation. In contrast, the formation of ethylene through the HO−C bond cleavage in the same C_2 intermediate does not involve direct interaction with the 3d spins in CuO. Thus, our experiment demonstrates the MF effect (MFE) in promoting electrochemical CO_2RR toward ethanol over ethylene catalyzed at a paramagnetic CuO surface.

RESULTS AND DISCUSSION

We first coated a 400 nm-thick Cu layer on the surface of a nanofibril polytetrafluoroethylene (PTFE) film via physical vapor deposition, followed by an oxygen-plasma treatment to convert the top Cu layer to CuO. This process creates a layered CuO/Cu nanofiber structure (Figures 1a and S1a). Energy-dispersive spectroscopy (EDS) demonstrated that both Cu and O were overlapped and uniformly distributed on the surface of the PTFE nanofibers (Figures 1b and S1b−d). High-resolution transmission electron microscopy (HRTEM) showed the Cu/CuO interfacial region (Figure 1c). While crystalline copper was found on the Cu side with a lattice fringe of 0.21 nm matching well with the *d*-spacing of the (111) crystal plane, the oxide region consisted of randomly aligned CuO nanocrystallites, amorphous CuO nanocrystallites, as well as Cu nanocrystallites. The lattice fringes of 0.16 and 0.25 nm correspond to the (202) and (002) crystal plane of CuO nanocrystallites, respectively. The lattice fringe of 0.21 nm matches with the (111) crystal plane of Cu nanoparticles. The powder X-ray diffraction (XRD) pattern (Figure S2) showed the presence of Cu metal but no crystalline CuO peak. This could be attributed to the amorphous nature of the CuO layer on the surface,[17] as observed by TEM. The oxidation state of the catalyst layer was determined by high-resolution X-ray photoelectron spectroscopy (XPS) at Cu 2*p* (Figure 1d) and O 1*s* transition (Figure S3). The XPS fine spectrum of Cu 2*p* (Figure 1d) of CuO/Cu depicts Cu 2*p*3/2 (~933.6 eV) and Cu 2*p*1/2 (~953.6 eV) with a gap difference of ~20 eV, which demonstrates the formation of CuO.[18,19] The peaks of the fitted curve at 932.7 eV (Cu 2*p*3/2) and 952.6 eV (Cu 2*p*1/2) can be assigned to the Cu (0) state, and the peaks at 934.3 eV (Cu 2*p*3/2) and 954.4 eV (Cu 2*p*1/2) are due to the Cu (+2) state.[17,20−22] Three satellite peaks are observed at around 941.3 eV, 943.7, and 962.1 eV, which reveal partially

https://doi.org/10.1021/jacs.6c05085
J. Am. Chem. Soc. XXXX, XXX, XXX−XXX

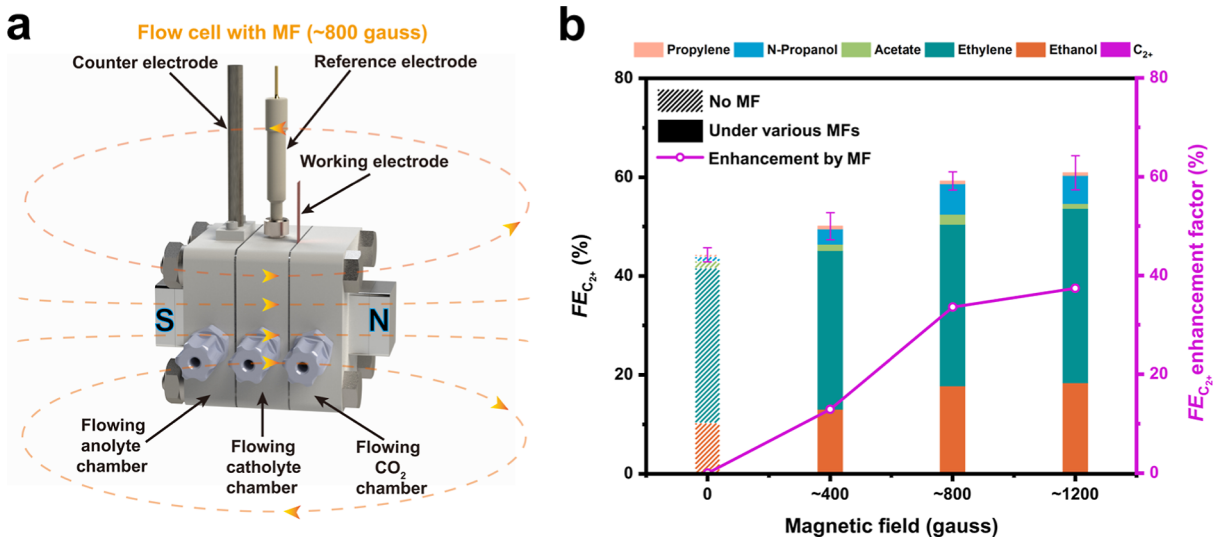

Figure 2. FE factor comparisons of the CuO/Cu catalyst with/without MF. (a) Scheme of a standard flow cell assembly with MF (~800 gauss). (b) FE_{C2+} on CuO/Cu at 100 mA/cm^2 without MF (oblique line bars) and with MFs of ~400 gauss, 800 gauss, and 1200 gauss (solid bars). The right coordinate denotes the FE enhancement factor toward C_{2+} products under different MFs. The error bars stand for one standard deviation of three independent measurements for FE_{C2+}.

filled d-block ($3d^9$) of the Cu^{2+} ions and are characteristic to the CuO electronic structure.[23] The O 1*s* spectrum of CuO/Cu in Figure S3 is deconvoluted into three peaks of the binding energy of ~529.7, 531.3, and 532.1 eV, which can be attributed to the lattice oxygen ($O_{lattice}$), oxygen vacancy ($O_{vacancy}$), and the surface-adsorbed oxygen ($O_{absorbed}$), respectively.[24] The paramagnetism of CuO/Cu on PTFE was confirmed by electron paramagnetic resonance (EPR) spectroscopy (Figure 1e). The observed resonance signal around 3293.596 gauss (g = 2.0347) is attributed to the paramagnetic Cu^{2+} ion arising from the electron configuration of $3d^9$ of CuO,[25−27] whereas a signal around 3340.470 gauss (g = 2.006) is assigned to the O^{2-} ions,[28,29] respectively. No paramagnetic signal is observed for the bare PTFE film, confirming the absence of unpaired spins. Importantly, EPR directly probes the Zeeman splitting of localized spins under an external magnetic field according to $\Delta E = g\,\mu_B B$, where μ_B is the Bohr magneton and B is the applied magnetic field. The resonance condition therefore reflects the alignment of the Cu^{2+} magnetic moments with the external magnetic field. The appearance and field-dependent position of the resonance peak provide direct spectroscopic evidence that localized Cu^{2+} spins are polarized by the applied magnetic field. To further quantify the magnetic moment response, magnetization versus magnetic field (M−H) measurements were performed at 300 K using MPMS (Figure 1f). The absence of hysteresis reconfirms the paramagnetic nature of CuO. As the external magnetic field strengthens, the magnetization of CuO/Cu on the PTFE sample continuously increases due to the alignment of the atomic magnetic moments in the sample with the direction of the external magnetic field. The magnetization saturates at about 1000 gauss, indicating near-complete polarization of the paramagnetic spins at room temperature. In contrast, the bare PTFE film does not exhibit any magnetization. Together, the EPR (microscopic Zeeman splitting of localized spins) and the MPMS M−H (macroscopic magnetization evolution) measurements provide complementary and quantitative evidence that the magnetic moments in CuO are reoriented and polarized under an external magnetic field. These measurements directly demonstrate magnetic moment modulation without requiring spatially resolved magnetometry.

We then conducted the CO_2RR study over the CuO/Cu electrode in a 1 M KOH electrolyte solution using a flow cell (Figures S4 and S5) with the configuration similar to that in a previous report.[30] Zero to three pairs of permanent SmCo magnets (Figures S6 and 2a) were incrementally applied to the flow cell to provide the magnetic flux density up to ~1200 gauss normal to the electrode surface. As shown in Figure 2b, the FE toward C_{2+} production (FE_{C2+}) on CuO/Cu rises under increased magnetic flux density from 50.1 ± 2.7% at ~400 gauss to 59.2 ± 1.9% at ~800 gauss and to 60.9 ± 3.5% at ~1200 gauss. The close values of FE_{C2+} at ~800 gauss and ~1200 gauss correlate with the magnetization measurements, where the degree of spin alignment in the CuO/Cu saturates at around 1000 gauss. To quantify the MFE on FE_{C2+}, we define the enhancement factor as the ratio of different FE_{C2+} with and without the external MF. The dotted purple curve in Figure 2b shows that the C_{2+} conversions are enhanced by ~12.9%, ~33.6%, and ~37.4% under external MFs of ~400 gauss, 800 gauss, and 1200 gauss, respectively.

To further probe the intrinsic electrocatalytic activity changes under a magnetic field, linear sweep voltammetry (LSV) was conducted on CuO/Cu and pure Cu electrodes with and without an external magnetic field of ~800 gauss (Figure S7a). The CuO/Cu electrode exhibited a markedly enhanced cathodic current density under the magnetic field. In contrast, the diamagnetic Cu electrode showed negligible response, indicating that the magnetic field predominantly affects spin-active surfaces such as CuO. Under an Ar atmosphere, where only the HER occurs, the LSV curves remain nearly identical with and without the magnetic field for both CuO/Cu and pure Cu electrodes, indicating that the magnetic field does not appreciably affect mass transport (Figure S7b). To verify the relevance of the magnetic field to CO_2RR, CO_2 reduction tests were performed on pure diamagnetic Cu electrodes at 100 mA/cm^2 with and without an external MF of ~800 gauss. As shown in Figure S8, the diamagnetic Cu electrodes demonstrated an FE_{C2+} of 40.0 ±

https://doi.org/10.1021/jacs.6c05085
J. Am. Chem. Soc. XXXX, XXX, XXX−XXX

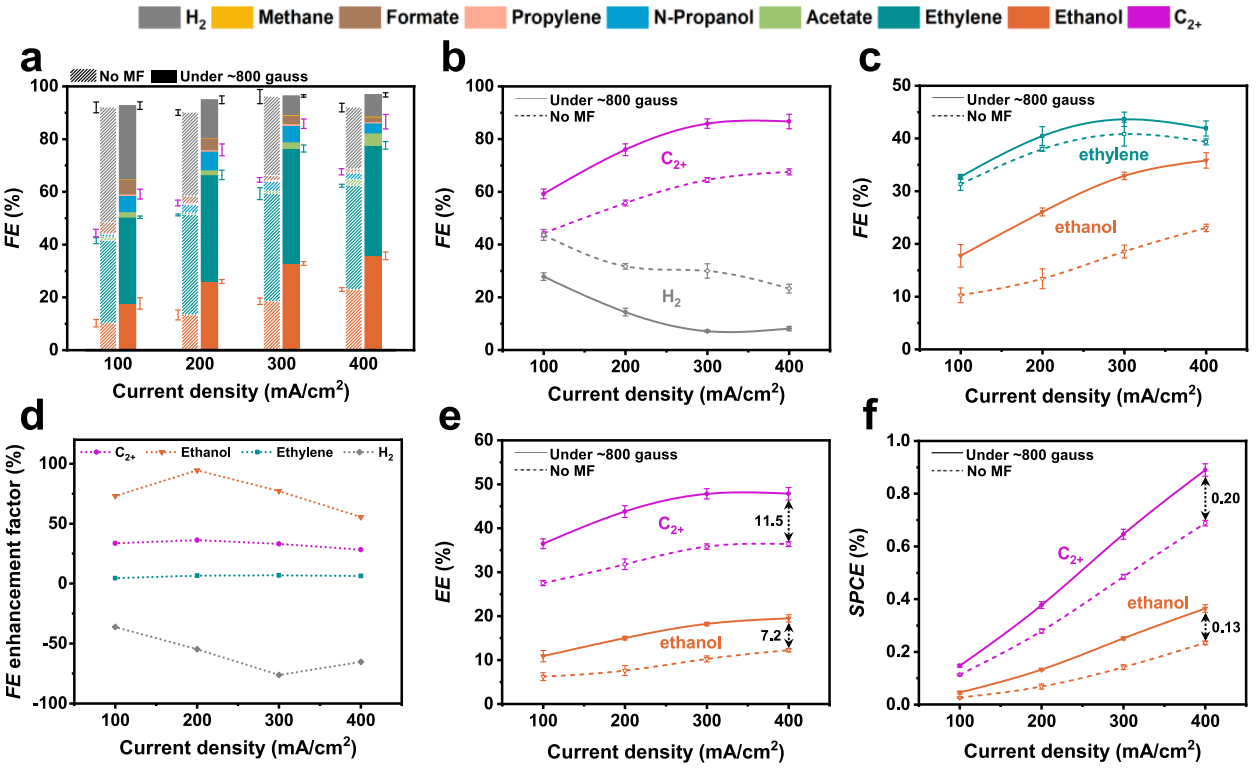

Figure 3. FE, EE, and SPCE comparisons of the CuO/Cu catalyst with/without the MF (~800 gauss). (a) FEs of total products at different current densities with (solid bars) and without (oblique line bars) the MF. (b) FE comparisons of C_{2+} products (magenta) and H_2 (gray). (c) FEs of ethanol (orange) and ethylene (aqua) with and without the MF at different current densities. (d) FE enhancement factors toward different CO_2RR products at varying current densities. (e) EE and (f) SPCE toward C_{2+} (magenta) and ethanol (orange) with and without the MF at different current densities. All the plots represent mean values and standard error bars from three replicate measurements.

5.5% in the absence of MF, statistically identical to 40.4 ± 3.2% obtained under ~800 gauss. The corresponding FE_{C2+} enhancement is merely ~1.08%, indicating no effect on the diamagnetic Cu surface. This comparison clearly indicates that a spin-polarized paramagnetic surface is relevant to the promoted FE_{C2+}. In addition, nonfaradaic CV measurements reveal that the double-layer capacitances (C_{dl}) of both Cu and CuO/Cu electrodes remain essentially unchanged in the presence and absence of the magnetic field, thereby excluding variations in electrochemically active surface area or interfacial charge accumulation as the origin of the observed enhancement (Figure S9).

To gain a better understanding of the relationship between current density and FE under the MFE, we investigated CO_2RR on CuO/Cu over a current density range from 100 mA/cm^2, 200 mA/cm^2, and 300 mA/cm^2 to 400 mA/cm^2, while maintaining the MF at ~800 gauss (Figure 3a). As shown in Figure 3b, the FE_{C2+} on CuO/Cu under the MF is consistently higher than that in the absence of the MF and increases with current density from 100 mA/cm^2 to 400 mA/cm^2. Meanwhile, the FE for hydrogen production (FE_{H2}) is significantly suppressed under the MF across all current densities, decreasing to 27.8 ± 1.4%, 14.3 ± 1.5%, 7.1 ± 0.4%, and 8.1 ± 0.8% at 100 mA/cm^2, 200 mA/cm^2, 300 mA/cm^2, and 400 mA/cm^2, respectively. These values are substantially lower than those obtained without the MF.

To further evaluate the impact of the MFE on C_{2+} product distribution, we analyzed the FEs of the two main products, ethanol and ethylene with and without an external MF of ~800 gauss (Figure 3c). As the current density increases, the FE for ethanol ($FE_{ethanol}$) rises from 10.3 ± 1.4%, 13.4 ± 1.9%, 18.6 ± 1.2%, and 23.0 ± 0.7% in the absence of MF to 17.8 ± 2.1%, 26.1 ± 0.8%, 32.9 ± 0.7%, and 35.8 ± 1.5% with the presence of MF at current densities of 100 mA/cm^2, 200 mA/cm^2, 300 mA/cm^2, and 400 mA/cm^2, respectively. Correspondingly, the partial current density (j) toward ethanol ($j_{ethanol}$) increases from 10.3 ± 1.4 mA/cm^2, 26.8 ± 3.7 mA/cm^2, 55.7 ± 3.6 mA/cm^2, and 92.1 ± 2.8 mA/cm^2 in the absence of MF to 17.8 ± 2.1 mA/cm^2, 52.1 ± 1.5 mA/cm^2, 98.7 ± 2.1 mA/cm^2, and 143.3 ± 5.8 mA/cm^2 in the presence of MF (Figure S10a). In contrast, the MFE on the partial current density toward ethylene ($j_{ethylene}$, Figure S10b) is relatively weak. The FE for ethylene ($FE_{ethylene}$) shows much weaker response to MFE (Figure 3c). As summarized in Table S1, a clear increase in the $FE_{ethanol}$ to $FE_{ethylene}$ ($FE_{ethanol}/FE_{ethylene}$) ratio is observed under the MF, indicating a preferential enhancement of ethanol selectivity over ethylene during CO_2RR. Figure 3d quantifies the enhancement factors on FE of the CO_2RR over CuO/Cu at various current densities at ~800 gauss. The specific enhancement factor for ethanol ranges between 55.6 and 94.5% in the applied current densities from 100 mA/cm^2 to 400 mA/cm^2, whereas little change occurs in that of ethylene (4.5−6.8%). Concurrently, H_2 formation is suppressed by −36.2% to −76.3% under the similar conditions. It is clear that MFE promotes the production of C_{2+} at the expense of H_2 generation, a desirable outcome of CO_2RR.

Energy efficiency (EE) is an important indicator to evaluate the cathodic energy efficiency of CO_2RR, assuming that the corresponding anodic oxygen evolution reaction (OER) is at the theoretic threshold.[31−33] Similar to the trends observed in FE, the MFE enhances the EE toward ethanol and C_{2+} products across the investigated current density range. At

https://doi.org/10.1021/jacs.6c05085
J. Am. Chem. Soc. XXXX, XXX, XXX−XXX

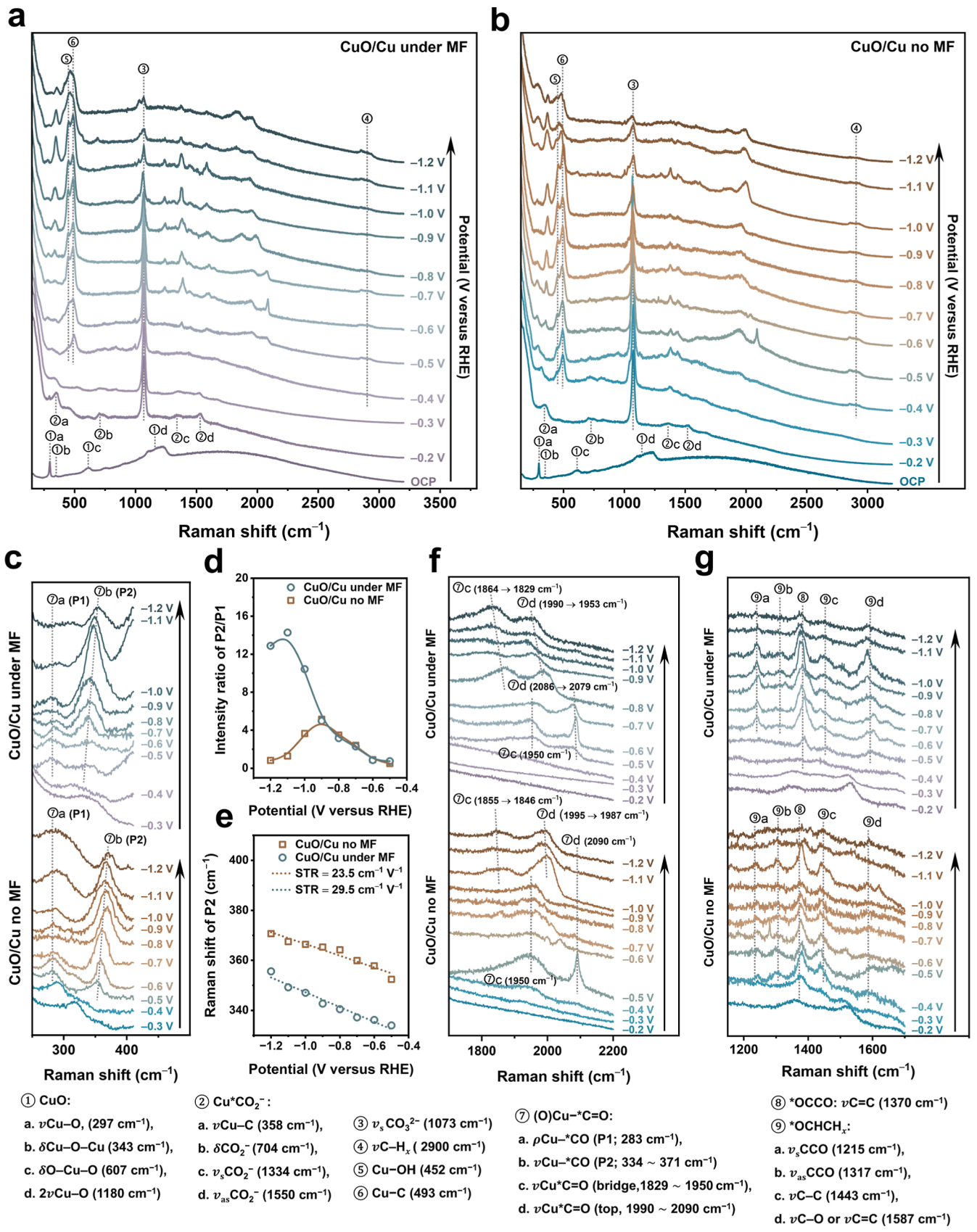

Figure 4. In situ SERS reveals magnetic-field-dependent CO_2RR pathways on CuO/Cu. In situ SERS spectra of CuO/Cu during CO_2 electroreduction recorded (a) with and (b) without an external MF. (c) Low-frequency SERS region showing two vibrational modes of Cu−*CO (P1 and P2). (d) P2/P1 ratio as a measure of surface *CO coverage at different cell potentials with and without MF. (e) Potential-dependent Cu−*CO vibrational shifts and STR with and without MF. (f) *C═O stretching region of Cu*C═O species with and without MF. (g) Spectra of key C_{2+} intermediates on CuO/Cu with and without MF.

https://doi.org/10.1021/jacs.6c05085
J. Am. Chem. Soc. XXXX, XXX, XXX−XXX

400 mA/cm^2, $EE_{ethanol}$ and EE_{C2+} increased by ~ 7.2% and ~11.5%, respectively (Figure 3e). Clearly, the majority of the EE_{C2+} increment is contributed by ethanol. Remarkably, through this simple physical method, namely, the MFE, the EE_{C2+} on CuO/Cu catalysts is promoted to 47.9 ± 1.4% at 400 mA/cm^2 over the 36.4 ± 0.6% at 400 mA/cm^2 in the absence of MFE.

From CO_2RR electrolyzer design point of view, high single-pass carbon efficiency (SPCE) is highly important in reducing the separation step for the converted product and its associated energy consumption.[3,34,35] By far, high SPCEs reported in the acidic systems account for the fact that the acids prevent the carbonate formation and its crossover in bulk electrolytes.[3,34,35] Though the SPCEs in alkaline systems were relatively low,[36,37] a strong basic electrolyte using KOH can bring higher selectivity and EE for C_{2+} production.[38] Therefore, enhancing SPCE via the MFE is of significant interest. The CuO/Cu catalyst exhibits improved SPCE toward ethanol under MFE (Figure 3f), which also contributes to an overall increase in SPCE for C_{2+} products across the current density range from 100 mA/cm^2 to 400 mA/cm^2. For instance, ~0.13% and ~0.2% improvement in SPCE was found, respectively, toward ethanol and overall C_{2+} chemicals, respectively, at 400 mA/cm^2 in the presence of the MF of ~800 gauss over that in the absence of MF. Apparently, 65% of the total SPCE increase for C_{2+} products is contributed to the enhanced single-pass efficiency of ethanol.

Furthermore, Figure S11 visualizes four key important indicators (i.e., FE, j, EE, and SPCE) toward C_{2+} (the magenta homocentric square) and ethanol (the orange homocentric square) production on CuO/Cu catalysts with/without an external MF of ~800 gauss at 400 mA/cm^2. A systematic improvement in FE_{C2+}, j_{C2+}, EE_{C2+}, and $SPCE_{C2+}$ is clearly observed under the MF. Ethanol represents the largest contributor to the increase of these four indicators. Under the MF, the CuO/Cu catalyst achieves an FE_{C2+} of 86.7 ± 2.7% at 400 mA/cm^2, representing a significant advancement compared to previously reported eCO_2RR performance on $Cu_{2-x}O$ catalysts (Table S2). The MFE simultaneous produced favorable FE_{C2+} in comparison with other chemical methods.

Furthermore, to elucidate how the external MF modulates the CO_2RR pathway, we performed in situ surface-enhanced Raman spectroscopy (SERS) on the CuO/Cu catalyst under reaction conditions with and without MF (Figure 4a,b). At open-circuit potential (OCP), both spectra exhibit prominent CuO lattice bands (Species 1 = νCu−O, 297 cm^{-1}; δCu−O−Cu, 343 cm^{-1}; δO−Cu−O, 607 cm^{-1}; and 2νCu−O, 1180 cm^{-1}) from the oxidized copper surface.[39] Reducing cathodic potential slightly from −0.2 to −0.4 V, characteristic bands of a carboxylate intermediate (*CO_2^-), formed via electron transfer from Cu to adsorbed CO_2, appear at 358 cm^{-1}, 704 cm^{-1}, 1334 cm^{-1}, and 1550 cm^{-1} in both spectra, assigned to the νCu−C, in-plane δCO_2^-, and symmetric and asymmetric O−C−O stretching of the *CO_2^- adsorbate, respectively (Species 2).[40,41] Simultaneously, a $\nu_s CO_3^{2-}$ band near 1070 cm^{-1} (Species 3) and a broad C−H stretching envelope at 2900 cm^{-1} (Species 4) appear as cell potential reached −0.4 V. Upon reaching −0.4 V, the intensities of two vibrational modes at ~452 cm^{-1} (Species 5) and 493 cm^{-1} (Species 6) grow with cathodic potentials, reaching a maximum around −0.8 V to −1.0 V. They are attributed to Cu−OH and Cu−C vibrations, respectively.[42]

As the cathodic potential grew more negative (≤−0.5 V), two low-frequency features appear at 283 cm^{-1} and 334 cm^{-1}−371 cm^{-1} (Species 7) over the catalyst in the presence and absence of the MF (Figure 4c). The lower-frequency peak corresponds to the frustrated rotation of adsorbed *CO (commonly known as P1), and the higher-frequency peak corresponds to the Cu−*CO stretch (commonly known as P2), as were observed in the previous studies on Cu surfaces.[43] As cathodic potential increases, P2 blue-shifted to higher wavenumber, reflecting the vibrational Stark effect under growing electric field, whereas P1 barely shifted. According to prior study,[43] the intensity ratio of P2/P1 serves as a proxy for surface *CO coverage,[43] as suggested by previous in situ Raman studies that higher ratios correlated with *CO-rich on Cu surfaces.[44] With or without the MF, this ratio rises with the cathodic potential, indicating an increase in *CO coverage (Figure 4d). Interestingly, the P2/P1 ratio rises more rapidly above −0.9 V under the MF than that without MF. This divergence signals that the MF promotes *CO accumulation on the CuO/Cu surface, consistent with the enhanced C_{2+} product yield. Our observation therefore revealed that the *CO coverage is enriched by MF at the catalyst surface, a key intermediate for enhanced C−C coupling. Furthermore, the Stark effect of the Cu−*CO was evaluated over the potential range from −0.5 to −1.2 V and found a stronger shift under MF (~29.5 cm^{-1} V^{-1}) than that without (~23.5 cm^{-1} V^{-1}) (Figure 4e). Higher Stark tuning rate (STR) implies an enhanced Cu−*CO bond dipole alignment under MF bond polarization, possibly through spin polarization at the CuO/Cu interface.

The *C═O stretch of Cu−*CO falls within 1800 cm^{-1}−2100 cm^{-1} (Figure 4f). At −0.5 V without a MF, two bands near 2090 cm^{-1} and 1950 cm^{-1} were assigned to weakly atop bound *C═O and strongly bridge bound *C═O on Cu, respectively.[45] As the cell potential becomes more cathodic, the weak 2090 cm^{-1} feature vanishes at −0.9 V, while the ~1950 cm^{-1} band remains. At a very negative potential of ≤ −1.0 V, this band splits into two bands (1995 cm^{-1} and 1855 cm^{-1}), reflecting highly back-bonded bridge *C═O on low-coordination sites. Under a MF, the corresponding vibrational bands behave differently. The bandwidth of the higher frequency band (2086 cm^{-1}) appeared at −0.5 V becomes broader, whereas the lower frequency band red-shifts substantially from 1953 cm^{-1} to 1829 cm^{-1} as the cell potential reaches −1.2 V. Such pronounced softening of the *C═O stretch is a direct sign of enhanced π back-bonding from Cu into CO antibonding orbitals. In other words, the field increases the electron density on Cu available for back-bonding, which lengthens/weaker the *C═O bond. This interpretation is consistent with the idea that atop *CO generally appears in the ~2000 cm^{-1}−2100 cm^{-1} range and bridge *CO in ~1800−1900 cm^{-1}; under field, both shift downward, emphasizing a higher degree of back-bonding. The magnetic field thus drives *C═O into more strongly bound, lower-frequency states that favor C−C coupling over desorption.

As the *CO coverage increases from −0.4 V to −1.2 V, new bands emerge in the 1200 cm^{-1}−1600 cm^{-1} region (Figure 4g). At 1370 cm^{-1}, we observed the signature peak of a protonated *CO dimer (*OCCO) intermediate (Species 8).[46] Meanwhile, four new peaks at 1215 cm^{-1} (Species 9a), 1317 cm^{-1} (Species 9b), 1443 cm^{-1} (Species 9c), and 1587 cm^{-1} (Species 9d) appear at more cathodic potentials, matching that

https://doi.org/10.1021/jacs.6c05085
J. Am. Chem. Soc. XXXX, XXX, XXX−XXX

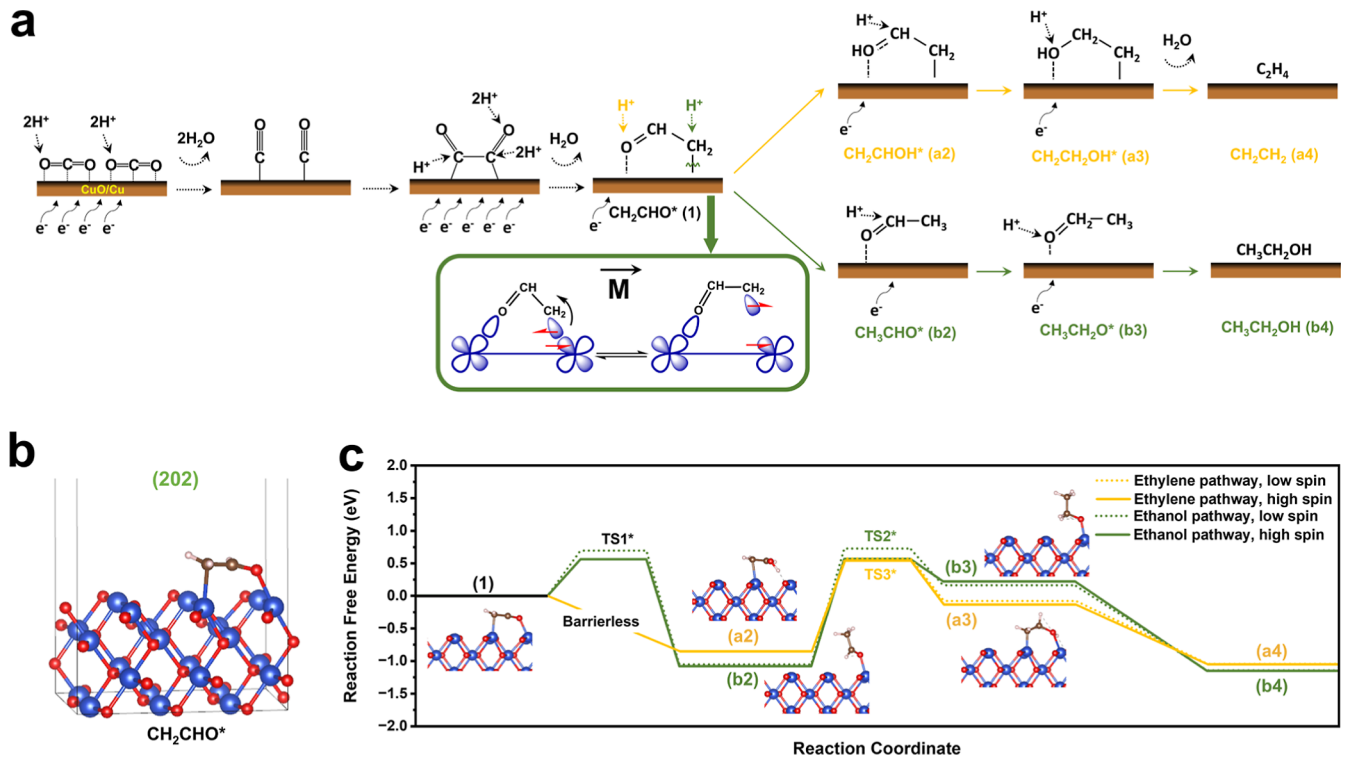

Figure 5. DTF calculations. (a) Schematic of the reaction pathways for ethanol and ethylene formation. (b) CH_2CHO adsorption over the CuO (202) surface. (c) Free energy diagram of CO_2RR over CuO forming ethylene (orange) and ethanol (green) with consideration of low (dashed line) and high (solid line) spin states. Color code: blue—Cu, red—O, brown—C, and white—H.

of known vibrational fingerprints of an ethanol-forming intermediate CH_xCHO^* (where x = 2 or 3, νCCO, ν_{as}CCO, νC−C, νC−O, or νC═C).[47] Notably, all four peaks intensify when MF is on, indicating that the field causes the increase of the intermediate population of $^*OCHCH_x$ on CuO/Cu.

Previous experimental and theoretical studies have established that the CO_2RR involves several key steps,[48−60] including CO_2 adsorption, deoxygenation, and reduction to CO, CO coupling, and subsequent hydrogenation via proton-coupled electron transfer (PCET) of $(CO)_2$ fragment as illustrated in the first four panels of Figure 5a. Our in situ Raman measurements reveal a long-lived species of CH_2CHO^* (**1**), which is considered as a possible pivotal intermediate for both ethanol[47] and ethylene formation. Thereafter, the reaction diverts into two distinct pathways.[58−60] In the ethylene pathway, the O atom in CH_2CHO^* undergoes hydrogenation via PCET to form CH_2CHOH^* (**a2**), followed by further hydrogenation at the adjacent C atom (**a3**). Subsequent PCET at the O atom leads to C−O bond cleavage and the release of C_2H_4 molecule (**a4**), completing a 12-electron PCET process. Notably, this pathway does not involve C−Cu bond cleavage throughout the hydrogenation sequence. In stark contrast, the ethanol pathway is initiated by C−Cu bond cleavage (denoted by the green panel in Figure 5a), accompanied by hydrogenation of the C atom initially bound to CuO, forming CH_3CHO^* (**b2**). The cleavage of the C−Cu bond results in two unpaired electrons, which align with the external magnetic field, leading to a stabilization energy of $-\mu_M B$ for each unpaired electron, where $-\mu_M$ is the magnetic moment of the electron spin and B is the magnetic flux density. An alternative understanding is that considering the reverse reaction, namely, the C−Cu bond formation in the $-CHOCH_2-(CuO)$ fragment, the two spins must have opposite directions. However, flipping one of the spins inevitably involves a challenging magnetic entropy change under magnetic field for this reverse reaction, causing high activation energy for the reverse reaction. Hence, the subsequent formation of CH_3CHO^* (**b2**) resulting from the hydrogenation of the C atom adjacent to CuO is promoted by the magnetic field. Subsequent hydrogenation on the C atom adjacent to the O atom in CH_3CHO^* (**b2**) leads to the formation of $CH_3CH_2O^*$ (**b3**). A final hydrogenation on the O atom of $CH_3CH_2O^*$ (**b3**) leads to the release of molecular ethanol (**b4**), completing this 12 PCET reaction. Although additional pathways can lead to other minor products such as acetate and propylene, the two pathways illustrated in Figure 5a govern the formation of the primary products, i.e., ethanol and ethylene, which are the focus of this study in relation to the MFE.

To further understand the magnetic effect on the selectivity of ethanol vs ethylene formation, first-principles density functional theory (DFT) calculations were performed to investigate the CO_2 reduction mechanism on the CuO (202) facet (Figure 5b) under an external MF. Based on prior reports,[58−60] CH_2CHO^* (Figure 5a) is a key intermediate following C−C coupling in the formation pathways of both ethylene and ethanol, and it was also identified in our in situ Raman spectra. Therefore, this species was selected as the starting point for mechanistic analysis, indicated by Figure 5a. Both low-spin and high-spin states were considered to represent the absence and presence of a magnetic field, respectively. In the low-spin configuration, the Cu magnetic moments have both spin-up and spin-down contributions, resulting in a near-zero total magnetic moment, whereas the high spin state comprises only spin-up magnetic moments on Cu atoms.

https://doi.org/10.1021/jacs.6c05085
J. Am. Chem. Soc. XXXX, XXX, XXX−XXX

As shown in Figure 5c, the free energy profile for the ethylene pathway indicates that the PCET to the oxygen atom of CH_2CHO^* to form CH_2CHOH^* (**a2**) is barrierless in both high- and low-spin states. The subsequent PCET of CH_2CHOH^* (**a2**) to form $CH_2CH_2OH^*$ (**a3**) exhibits a kinetic barrier of 1.42 eV (TS3*, Figure S12a) at the low-spin state, which decreases slightly to 1.39 eV in the high-spin state. In contrast, for ethanol formation, the PCET of the terminal carbon of CH_2CHO^* to form CH_3CHO^* (**b2**) shows a kinetic barrier of 0.70 eV (TS1*, Figure S12b) at the low-spin state, followed by the PCET of CH_3CHO^* (**b2**) with a barrier of 1.78 eV (TS2*, Figure S12c). Under high-spin conditions, these barriers decrease to 0.56 and 1.65 eV, respectively. Although the magnetic field has an impact on reaction kinetics, the reaction thermodynamics are barely changed in all cases. Overall, comparison of the free energy profiles indicates that the magnetic field lowers hydrogenation barriers, with the ethanol pathway showing greater sensitivity; nevertheless, the ethylene pathway remains more favorable, consistent with the experimental observations in Figure 3. It is worth highlighting that the magnetic field promotes the hydrogenation of the terminal carbon of CH_2CHO^* to form CH_3CHO^*, inducing $Cu-C_{terminal}$ bond cleavage. Considering implicit solvation and external potential bias, similar trends still hold (Figure S13).

CONCLUSIONS

We demonstrated that a moderate external magnetic field (~800 gauss) can alter the spin-dependent reaction pathways in electrochemical CO_2RR on a paramagnetic, conductive CuO surface by polarizing the spins of the two unpaired electrons generated during C−Cu bond cleavage in the organic intermediate, thereby influencing its dissociation kinetics at the organic−CuO interface. This behavior may also be viewed as the spin state of the intermediate being perturbed by the external magnetic field during its evolution. Under the magnetic field, the CO_2-to-C_{2+} FE increased by ~30% to 86.7 ± 2.7%, with an EE of 47.9 ± 1.4% at 400 mA/cm^2. Impressively, ethanol formation exhibited a notably higher magnetic response (~55.6% increase in FE) than ethylene (~6.4%), indicating a shift in selectivity. DFT calculations suggest that the external magnetic field has a noticeable impact on the reaction kinetic barriers toward ethanol formation, while only minor impact on the ethylene formation barriers was observed. Meanwhile, the reaction thermodynamics remain largely unchanged. In situ SERS performed during CO_2 electroreduction on the CuO/Cu surface revealed that the magnetic field enriches surface *CO coverage, strengthens Cu−CO back-bonding, and increases the steady-state population of ethanol-forming $*OCHCH_x$ intermediates, thereby providing direct spectroscopic evidence for magnetic-field-modulated reaction pathways. These findings establish a mechanistic basis for magnetic-field-enhanced electrocatalysis and highlight a promising strategy for modulating product selectivity in CO_2 electrosynthesis.

ASSOCIATED CONTENT

Supporting Information

The Supporting Information is available free of charge at https://pubs.acs.org/doi/10.1021/jacs.6c05085.

Experimental section; STEM, XRD, and XPS characterization of the CuO/Cu electrode; schematic illustration of the flow cell with and without a MF; LSV curves of the Cu/Cu electrode; FE_{C2+} of the pure Cu electrode; partial current densities for ethanol and ethylene on the CuO/Cu electrode; comparation of C_{2+} (FE_{C2+}, j_{C2+}, EE_{C2+}, and $SPCE_{C2+}$) and ethanol ($FE_{ethanol}$, $j_{ethanol}$, $EE_{ethanol}$, and $SPCE_{ethanol}$) on CuO/Cu with and without a MF; DFT calculation; STEM image and elemental mapping; XRD patterns; high-resolution O 1*s* spectra; schematic view of the flow cell and a standard flow cell assembly; LSV curves; *FE*; cyclic voltammograms; partial current densities; comparison of C_{2+} and ethanol; optimized transition state structures; DTF calculations; values comparisons; and summary of CO_2 reduction to C_{2+} products performance (PDF)

AUTHOR INFORMATION

Corresponding Authors

Cong Liu − *Chemical Sciences and Engineering Division, Argonne National Laboratory, Lemont, Illinois 60439, United States;* orcid.org/0000-0002-2145-5034; Email: congliu@anl.gov

Di-Jia Liu − *Chemical Sciences and Engineering Division, Argonne National Laboratory, Lemont, Illinois 60439, United States; Pritzker School of Molecular Engineering, The University of Chicago, Chicago, Illinois 60637, United States;* orcid.org/0000-0003-1747-028X; Email: djliu@anl.gov

Tao Xu − *Department of Chemistry and Biochemistry, Northern Illinois University, DeKalb, Illinois 60115, United States;* orcid.org/0000-0002-3343-7263; Email: txu@niu.edu

Authors

Fujun Tao − *Department of Chemistry and Biochemistry, Northern Illinois University, DeKalb, Illinois 60115, United States; Chemical Sciences and Engineering Division, Argonne National Laboratory, Lemont, Illinois 60439, United States;* orcid.org/0000-0003-1156-842X

Jianxin Wang − *Department of Chemistry and Biochemistry, Northern Illinois University, DeKalb, Illinois 60115, United States; Chemical Sciences and Engineering Division, Argonne National Laboratory, Lemont, Illinois 60439, United States;* orcid.org/0009-0002-0410-5240

Jiayi Xu − *Chemical Sciences and Engineering Division, Argonne National Laboratory, Lemont, Illinois 60439, United States;* orcid.org/0000-0003-1763-6251

Guangji Chen − *Angstrom Advanced Inc., Stoughton, Massachusetts 02072, United States*

Xudong Xiao − *Department of Chemistry and Biochemistry, Northern Illinois University, DeKalb, Illinois 60115, United States*

Mengyuan Li − *Department of Chemistry and Biochemistry, Northern Illinois University, DeKalb, Illinois 60115, United States;* orcid.org/0009-0007-2549-1781

Haozhe Zhang − *Chemical Sciences and Engineering Division, Argonne National Laboratory, Lemont, Illinois 60439, United States;* orcid.org/0000-0001-6363-5271

Xinwei Zhou − *Center for Nanoscale Materials, Argonne National Laboratory, Lemont, Illinois 60439, United States*

Yuzi Liu − *Center for Nanoscale Materials, Argonne National Laboratory, Lemont, Illinois 60439, United States*

https://doi.org/10.1021/jacs.6c05085
J. Am. Chem. Soc. XXXX, XXX, XXX−XXX

Owen S. Wostoupal − *Department of Chemistry and Biochemistry, Northern Illinois University, DeKalb, Illinois 60115, United States;* orcid.org/0000-0002-4755-1569
Zhenzhen Yang − *Chemical Sciences and Engineering Division, Argonne National Laboratory, Lemont, Illinois 60439, United States;* orcid.org/0000-0002-1073-3799
Bing Shi − *Advanced Photon Source, Argonne National Laboratory, Lemont, Illinois 60439, United States*
H. Christopher Fry − *Center for Nanoscale Materials, Argonne National Laboratory, Lemont, Illinois 60439, United States;* orcid.org/0000-0001-8343-5189
John E. Pearson − *Center for Nanoscale Materials, Argonne National Laboratory, Lemont, Illinois 60439, United States*
Haiming Li − *Angstrom Advanced Inc., Stoughton, Massachusetts 02072, United States*
Chong Zheng − *Department of Chemistry and Biochemistry, Northern Illinois University, DeKalb, Illinois 60115, United States;* orcid.org/0000-0002-3681-305X

Complete contact information is available at: https://pubs.acs.org/10.1021/jacs.6c05085

Author Contributions

[¶]F. T., J. W., and J. X. contributed equally to this work.

Notes

The authors declare no competing financial interest.

■ ACKNOWLEDGMENTS

This work was supported by the U.S. Department of Energy's Office of Critical Minerals and Energy Innovation (CMEI) under the award number DE-EE0009418. Work performed at Argonne National Laboratory's Center for Nanoscale Materials (CNM), US DOE Office of Science User Facilities, was supported by the U.S. DOE, Office of Basic Energy Science, under Contract No. DE-AC02-06CH11357. J. W., H. Z., and D.-J. L. acknowledge the financial support from Laboratory Directed Research and Development (LDRD) funding from Argonne National Laboratory, provided by the Director, Office of Science, of the U.S. Department of Energy under Contract No. DE-AC02-06CH11357. D.J.L also acknowledges the financial support by the Department of Energy, Advanced Research Projects Agency-Energy (ARPA-E), under Award Number DE-AR0001948. The computational studies by J. X. and C. L. were supported by the U.S. Department of Energy (DOE), Office of Science (SC), Office of Basic Energy Sciences (BES), Division of Chemical Sciences, Geosciences and Biosciences (CSGB), Catalysis Science Program under contract No. DE-AC02-06CH11357. All the DFT calculations were carried out utilizing computational resources provided by the Laboratory Computing Research Center (LCRC) at the Argonne National Laboratory. Z. Y. acknowledges the support from Post Test Facility of Argonne National Laboratory, supported by Department of Energy, Vehicle Technologies Office, under Contract No. DE-AC02-06CH11357. Purchase of the NMR spectrometer used to obtain partial results included in this work was supported by the National Science Foundation under the MRI award CHE-2117776.

■ REFERENCES

(1) Gao, D.; Arán-Ais, R. M.; Jeon, H. S.; Roldan Cuenya, B. Rational catalyst and electrolyte design for CO_2 electroreduction towards multicarbon products. *Nat. Catal.* **2019**, *2* (3), 198−210.
(2) Zhang, X.; Li, J.; Li, Y.-Y.; Jung, Y.; Kuang, Y.; Zhu, G.; Liang, Y.; Dai, H. Selective and high current CO_2 electro-reduction to multicarbon products in near-neutral KCl electrolytes. *J. Am. Chem. Soc.* **2021**, *143* (8), 3245−3255.
(3) Zhao, Y.; Hao, L.; Ozden, A.; Liu, S.; Miao, R. K.; Ou, P.; Alkayyali, T.; Zhang, S.; Ning, J.; Liang, Y.; Xu, Y.; Fan, M.; Chen, Y.; Huang, J. E.; Xie, K.; Zhang, J.; O'Brien, C. P.; Li, F.; Sargent, E. H.; Sinton, D. Conversion of CO_2 to multicarbon products in strong acid by controlling the catalyst microenvironment. *Nat. Synth.* **2023**, *2* (5), 403−412.
(4) Rosen, B. A.; Salehi-Khojin, A.; Thorson, M. R.; Zhu, W.; Whipple, D. T.; Kenis, P. J. A.; Masel, R. I. Ionic liquid-mediated selective conversion of CO_2 to CO at low overpotentials. *Science* **2011**, *334* (6056), 643−644.
(5) Asadi, M.; Kim, K.; Liu, C.; Addepalli, A. V.; Abbasi, P.; Yasaei, P.; Phillips, P.; Behranginia, A.; Cerrato, J. M.; Haasch, R.; Zapol, P.; Kumar, B.; Klie, R. F.; Abiade, J.; Curtiss, L. A.; Salehi-Khojin, A. Nanostructured transition metal dichalcogenide electrocatalysts for CO_2 reduction in ionic liquid. *Science* **2016**, *353* (6298), 467−470.
(6) Gao, W.; Xu, Y.; Fu, L.; Chang, X.; Xu, B. Experimental evidence of distinct sites for CO_2-to-CO and CO conversion on Cu in the electrochemical CO_2 reduction reaction. *Nat. Catal.* **2023**, *6* (10), 885−894.
(7) Li, J.; Kuang, Y.; Meng, Y.; Tian, X.; Hung, W.-H.; Zhang, X.; Li, A.; Xu, M.; Zhou, W.; Ku, C.-S.; Chiang, C.-Y.; Zhu, G.; Guo, J.; Sun, X.; Dai, H. Electroreduction of CO_2 to formate on a copper-based electrocatalyst at high pressures with high energy conversion efficiency. *J. Am. Chem. Soc.* **2020**, *142* (16), 7276−7282.
(8) Küngas, R. Review-electrochemical CO_2 reduction for CO production: comparison of low- and high-temperature electrolysis technologies. *J. Electrochem. Soc.* **2020**, *167* (4), 044508.
(9) Staub, U.; Tanaka, Y.; Katsumata, K.; Kikkawa, A.; Kuramoto, Y.; Onuki, Y. Influence of stress and magnetic field on the orbital orientations in CeB_6. *J. Phys.: Condens. Matter* **2006**, *18* (48), 11007.
(10) Xu, J.; Wu, F.; Bao, J.-K.; Han, F.; Xiao, Z.-L.; Martin, I.; Lyu, Y.-Y.; Wang, Y.-L.; Chung, D. Y.; Li, M.; Zhang, W.; Pearson, J. E.; Jiang, J. S.; Kanatzidis, M. G.; Kwok, W.-K. Orbital-flop induced magnetoresistance anisotropy in rare earth monopnictide CeSb. *Nat. Commun.* **2019**, *10* (1), 2875.
(11) Pan, H.; Jiang, X.; Wang, X.; Wang, Q.; Wang, M.; Shen, Y. Effective magnetic field regulation of the radical pair spin states in electrocatalytic CO_2 reduction. *J. Phys. Chem. Lett.* **2020**, *11* (1), 48−53.
(12) Hao, J.; Xie, S.; Huang, Q.; Ding, Z.; Sheng, H.; Zhang, C.; Yao, J. Spin-enhanced C-C coupling in CO_2 electroreduction with oxide-derived copper. *CCS Chem.* **2023**, *5* (9), 2046−2058.
(13) Lin, C.-C.; Liu, T.-R.; Lin, S.-R.; Boopathi, K. M.; Chiang, C.-H.; Tzeng, W.-Y.; Chien, W.-H. C.; Hsu, H.-S.; Luo, C.-W.; Tsai, H.-Y.; Chen, H.-A.; Kuo, P.-C.; Shiue, J.; Chiou, J.-W.; Pong, W.-F.; Chen, C.-C.; Chen, C.-W. Spin-polarized photocatalytic CO_2 reduction of Mn-doped perovskite nanoplates. *J. Am. Chem. Soc.* **2022**, *144* (34), 15718−15726.
(14) Song, J.; He, D.; Ma, X.; Liu, P.; Guo, W.; Sun, R.; Li, F.; Zhong, Z.; Zhou, H.; Tang, J.; Xu, J.; Wu, T.; Hu, L.; Wu, Y. Magnetic Field-Enhanced Acidic CO_2 Electroreduction Reaction on Single Nickel-Site Catalysts. *J. Am. Chem. Soc.* **2025**, *147* (19), 16198−16206.
(15) Saglam, H.; Duzgun, A.; Kargioti, A.; Harle, N.; Zhang, X.; Bingham, N. S.; Lao, Y.; Gilbert, I.; Sklenar, J.; Watts, J. D.; Ramberger, J.; Bromley, D.; Chopdekar, R. V.; O'Brien, L.; Leighton, C.; Nisoli, C.; Schiffer, P. Entropy-Driven Order in an Array of Nanomagnets. *Nat. Phys.* **2022**, *18* (6), 706−712.
(16) Lee, W.-J.; Wang, X.-J. Structural, optical, and electrical properties of copper oxide films grown by the SILAR method with post-annealing. *Coatings* **2021**, *11* (7), 864.
(17) Xia, Y.; Zhang, Q.; Guo, F.; Wang, J.; Li, W.; Xu, J. Ag@Cu with Cu-CuO interface prepared by air cold-plasma promoting the electrocatalytic reduction of CO_2 to low-carbon alcohols. *Vacuum* **2022**, *196*, 110767.

(18) Selvanathan, V.; Aminuzzaman, M.; Tey, L.-H.; Razali, S. A.; Althubeiti, K.; Alkhammash, H. I.; Guha, S. K.; Ogawa, S.; Watanabe, A.; Shahiduzzaman, M.; Akhtaruzzaman, M. Muntingia calabura leaves mediated green synthesis of CuO nanorods: exploiting phytochemicals for unique morphology. *Materials* **2021**, *14* (21), 6379.
(19) Sudha, V.; Murugadoss, G.; Thangamuthu, R. Structural and morphological tuning of Cu-based metal oxide nanoparticles by a facile chemical method and highly electrochemical sensing of sulphite. *Sci. Rep.* **2021**, *11* (1), 3413.
(20) Hui, L. S.; Whiteway, E.; Hilke, M.; Turak, A. Synergistic oxidation of CVD graphene on Cu by oxygen plasma etching. *Carbon* **2017**, *125*, 500−508.
(21) Chusuei, C. C.; Brookshier, M. A.; Goodman, D. W. Correlation of Relative X-ray Photoelectron Spectroscopy Shake-up Intensity with CuO Particle Size. *Langmuir* **1999**, *15* (8), 2806−2808.
(22) Song, Y.; Cho, D.; Venkateswarlu, S.; Yoon, M. Systematic study on preparation of copper nanoparticle embedded porous carbon by carbonization of metal−organic framework for enzymatic glucose sensor. *RSC Adv.* **2017**, *7* (17), 10592−10600.
(23) Singh, B. P.; Chaudhary, M.; Kumar, A.; Singh, A. K.; Gautam, Y. K.; Rani, S.; Walia, R. Effect of Co and Mn doping on the morphological, optical and magnetic properties of CuO nanostructures. *Solid State Sci.* **2020**, *106*, 106296.
(24) Rajendran, K.; Yadav, J.; Khan, T. S.; Haider, M. A.; Gupta, S.; Jagadeesan, D. Oxygen vacancy-mediated reactivity: the curious case of reduction of nitroquinoline to aminoquinoline by CuO. *J. Phys. Chem. C* **2023**, *127* (18), 8576−8584.
(25) Sekhar, H.; Narayana Rao, D. Preparation, characterization and nonlinear absorption studies of cuprous oxide nanoclusters, microcubes and micro-particles. *J. Nanopart. Res.* **2012**, *14* (7), 976.
(26) Lin, K.-S.; Wang, H. P. Byproduct shape selectivity in supercritical water oxidation of 2-chlorophenol effected by CuO/ZSM-5. *Langmuir* **2000**, *16* (6), 2627−2631.
(27) Maurelli, S.; Ruszak, M.; Witkowski, S.; Pietrzyk, P.; Chiesa, M.; Sojka, Z. Spectroscopic CW-EPR and HYSCORE investigations of Cu^{2+} and O_2^- species in copper doped nanoporous calcium aluminate ($12CaO{\cdot}7Al_2O_3$). *Phys. Chem. Chem. Phys.* **2010**, *12* (36), 10933−10941.
(28) Che, M.; Tench, A. J. Characterization and reactivity of molecular oxygen species on oxide surfaces. In *Adv. Catal.*; Eley, D. D., Pines, H., Weisz, P. B., Eds.; Academic Press, 1983; Vol. *32*, pp 1−148.
(29) Sojka, Z. Molecular aspects of catalytic reactivity. Application of EPR spectroscopy to stuies of the mechanism of heterogeneous catalytic reactions. *Catal. Rev. - Sci. Eng.* **1995**, *37* (3), 461−512.
(30) Nguyen, T. N.; Chen, Z.; Zeraati, A. S.; Shiran, H. S.; Sadaf, S. M.; Kibria, M. G.; Sargent, E. H.; Dinh, C.-T. Catalyst regeneration via chemical oxidation enables long-term electrochemical carbon dioxide reduction. *J. Am. Chem. Soc.* **2022**, *144* (29), 13254−13265.
(31) Zhong, M.; Tran, K.; Min, Y.; Wang, C.; Wang, Z.; Dinh, C.-T.; De Luna, P.; Yu, Z.; Rasouli, A. S.; Brodersen, P.; Sun, S.; Voznyy, O.; Tan, C.-S.; Askerka, M.; Che, F.; Liu, M.; Seifitokaldani, A.; Pang, Y.; Lo, S.-C.; Ip, A.; Ulissi, Z.; Sargent, E. H. Accelerated discovery of CO_2 electrocatalysts using active machine learning. *Nature* **2020**, *581* (7807), 178−183.
(32) Peng, C.; Yang, S.; Luo, G.; Yan, S.; Shakouri, M.; Zhang, J.; Chen, Y.; Li, W.; Wang, Z.; Sham, T.-K.; Zheng, G. Surface Co-modification of halide anions and potassium cations promotes high-rate CO_2-to-ethanol electrosynthesis. *Adv. Mater.* **2022**, *34* (39), 2204476.
(33) Wen, G.; Ren, B.; Park, M. G.; Yang, J.; Dou, H.; Zhang, Z.; Deng, Y.-P.; Bai, Z.; Yang, L.; Gostick, J.; Botton, G. A.; Hu, Y.; Chen, Z. Ternary Sn-Ti-O electrocatalyst boosts the stability and energy efficiency of CO_2 reduction. *Angew. Chem., Int. Ed.* **2020**, *59* (31), 12860−12867.
(34) Huang, J. E.; Li, F.; Ozden, A.; Sedighian Rasouli, A.; García de Arquer, F. P.; Liu, S.; Zhang, S.; Luo, M.; Wang, X.; Lum, Y.; Xu, Y.; Bertens, K.; Miao, R. K.; Dinh, C.-T.; Sinton, D.; Sargent, E. H. CO_2 electrolysis to multicarbon products in strong acid. *Science* **2021**, *372* (6546), 1074−1078.
(35) Li, L.; Liu, Z.; Yu, X.; Zhong, M. Achieving high single-pass carbon conversion efficiencies in durable CO_2 electroreduction in strong acids via electrode structure engineering. *Angew. Chem. Int. Ed* **2023**, *62* (21), No. e202300226.
(36) García de Arquer, F. P.; Dinh, C.-T.; Ozden, A.; Wicks, J.; McCallum, C.; Kirmani, A. R.; Nam, D.-H.; Gabardo, C.; Seifitokaldani, A.; Wang, X.; Li, Y. C.; Li, F.; Edwards, J.; Richter, L. J.; Thorpe, S. J.; Sinton, D.; Sargent, E. H. CO_2 electrolysis to multicarbon products at activities greater than 1 A cm^{-2}. *Science* **2020**, *367* (6478), 661−666.
(37) Dinh, C.-T.; Burdyny, T.; Kibria, M. G.; Seifitokaldani, A.; Gabardo, C. M.; García de Arquer, F. P.; Kiani, A.; Edwards, J. P.; De Luna, P.; Bushuyev, O. S.; Zou, C.; Quintero-Bermudez, R.; Pang, Y.; Sinton, D.; Sargent, E. H. CO_2 electroreduction to ethylene via hydroxide-mediated copper catalysis at an abrupt interface. *Science* **2018**, *360* (6390), 783−787.
(38) Nitopi, S.; Bertheussen, E.; Scott, S. B.; Liu, X.; Engstfeld, A. K.; Horch, S.; Seger, B.; Stephens, I. E. L.; Chan, K.; Hahn, C.; Nørskov, J. K.; Jaramillo, T. F.; Chorkendorff, I. Progress and perspectives of electrochemical CO_2 reduction on copper in aqueous electrolyte. *Chem. Rev.* **2019**, *119* (12), 7610−7672.
(39) Litvinchuk, A. P.; Möller, A.; Debbichi, L.; Krüger, P.; Iliev, M. N.; Gospodinov, M. M. Second-order Raman scattering in CuO. *J. Phys.: Condens. Matter* **2013**, *25* (10), 105402.
(40) Zhao, Y.; Zhang, X.-G.; Bodappa, N.; Yang, W.-M.; Liang, Q.; Radjenovica, P. M.; Wang, Y.-H.; Zhang, Y.-J.; Dong, J.-C.; Tian, Z.-Q.; Li, J.-F. Elucidating electrochemical CO_2 reduction reaction processes on Cu(hkl) single-crystal surfaces by in situ Raman spectroscopy. *Energy Environ. Sci.* **2022**, *15* (9), 3968−3977.
(41) Chernyshova, I. V.; Somasundaran, P.; Ponnurangam, S. On the origin of the elusive first intermediate of CO_2 electroreduction. *Proc. Natl. Acad. Sci. U. S. A.* **2018**, *115* (40), E9261−E9270.
(42) Moradzaman, M.; Mul, G. In situ Raman study of potential-dependent surface adsorbed carbonate, CO, OH, and C species on Cu electrodes during electrochemical reduction of CO_2. *ChemElectroChem* **2021**, *8* (8), 1478−1485.
(43) Zhan, C.; Dattila, F.; Rettenmaier, C.; Bergmann, A.; Kühl, S.; García-Muelas, R.; López, N.; Cuenya, B. R. Revealing the CO coverage-driven C-C coupling mechanism for electrochemical CO_2 reduction on Cu_2O nanocubes via operando Raman spectroscopy. *ACS Catal.* **2021**, *11* (13), 7694−7701.
(44) Wang, S.; Li, F.; Zhao, J.; Zeng, Y.; Li, Y.; Lin, Z.-Y.; Lee, T.-J.; Liu, S.; Ren, X.; Wang, W.; Chen, Y.; Hung, S.-F.; Lu, Y.-R.; Cui, Y.; Yang, X.; Li, X.; Huang, Y.; Liu, B. Manipulating C-C coupling pathway in electrochemical CO_2 reduction for selective ethylene and ethanol production over single-atom alloy catalyst. *Nat. Commun.* **2024**, *15* (1), 10247.
(45) Ma, H.; Ibáñez-Alé, E.; You, F.; López, N.; Yeo, B. S. Electrochemical formation of C_{2+} products steered by bridge-bonded *CO confined by *OH domains. *J. Am. Chem. Soc.* **2024**, *146* (44), 30183−30193.
(46) Shao, F.; Wong, J. K.; Low, Q. H.; Iannuzzi, M.; Li, J.; Lan, J. In situ spectroelectrochemical probing of CO redox landscape on copper single-crystal surfaces. *Proc. Natl. Acad. Sci. U. S. A.* **2022**, *119* (29), No. e2118166119.
(47) Zhan, C.; Dattila, F.; Rettenmaier, C.; Herzog, A.; Herran, M.; Wagner, T.; Scholten, F.; Bergmann, A.; López, N.; Roldan Cuenya, B. Key intermediates and Cu active sites for CO_2 electroreduction to ethylene and ethanol. *Nat. Energy* **2024**, *9* (12), 1485−1496.
(48) Cai, R.; Sun, M.; Yang, F.; Ju, M.; Chen, Y.; Gu, M. D.; Huang, B.; Yang, S. Engineering Cu(I)/Cu(0) interfaces for efficient ethanol production from CO_2 electroreduction. *Chem* **2024**, *10* (1), 211−233.
(49) Cheng, T.; Xiao, H.; Goddard, W. A. Full atomistic reaction mechanism with kinetics for CO reduction on Cu (100) from ab initio molecular dynamics free-energy calculations at 298 K. *Proc. Natl. Acad. Sci. U. S. A.* **2017**, *114* (8), 1795−1800.

https://doi.org/10.1021/jacs.6c05085
J. Am. Chem. Soc. XXXX, XXX, XXX−XXX

(50) Lum, Y.; Cheng, T.; Goddard, W. A., III; Ager, J. W. Electrochemical CO reduction builds solvent water into oxygenate products. *J. Am. Chem. Soc.* **2018**, *140* (30), 9337−9340.
(51) Wang, X.; Wang, Z.; García de Arquer, F. P.; Dinh, C.-T.; Ozden, A.; Li, Y. C.; Nam, D.-H.; Li, J.; Liu, Y.-S.; Wicks, J.; Chen, Z.; Chi, M.; Chen, B.; Wang, Y.; Tam, J.; Howe, J. Y.; Proppe, A.; Todorović, P.; Li, F.; Zhuang, T.-T.; Gabardo, C. M.; Kirmani, A. R.; McCallum, C.; Hung, S.-F.; Lum, Y.; Luo, M.; Min, Y.; Xu, A.; O'Brien, C. P.; Stephen, B.; Sun, B.; Ip, A. H.; Richter, L. J.; Kelley, S. O.; Sinton, D.; Sargent, E. H. Efficient electrically powered CO_2-to-ethanol via suppression of deoxygenation. *Nat. Energy* **2020**, *5* (6), 478−486.
(52) Zhao, Q.; Martirez, J. M. P.; Carter, E. A. Charting C-C coupling pathways in electrochemical CO_2 reduction on Cu (111) using embedded correlated wavefunction theory. *Proc. Natl. Acad. Sci. U. S. A.* **2022**, *119* (44), No. e2202931119.
(53) Calle-Vallejo, F.; Koper, M. T. Theoretical considerations on the electroreduction of CO to C_2 species on Cu (100) electrodes. *Angew. Chem.* **2013**, *125* (28), 7423−7426.
(54) Goodpaster, J. D.; Bell, A. T.; Head-Gordon, M. Identification of possible pathways for C-C bond formation during electrochemical reduction of CO_2: new theoretical insights from an improved electrochemical model. *J. Phys. Chem. Lett.* **2016**, *7* (8), 1471−1477.
(55) Sandberg, R. B.; Montoya, J. H.; Chan, K.; Nørskov, J. K. CO-CO coupling on Cu facets: coverage, strain and field effects. *Surf. Sci.* **2016**, *654*, 56−62.
(56) Xiao, H.; Cheng, T.; Goddard, W. A., III; Sundararaman, R. Mechanistic explanation of the pH dependence and onset potentials for hydrocarbon products from electrochemical reduction of CO on Cu (111). *J. Am. Chem. Soc.* **2016**, *138* (2), 483−486.
(57) Xiao, H.; Cheng, T.; Goddard, W. A., III Atomistic mechanisms underlying selectivities in C_1 and C_2 products from electrochemical reduction of CO on Cu (111). *J. Am. Chem. Soc.* **2017**, *139* (1), 130−136.
(58) Wong, A. J.-W.; Tran, B.; Agrawal, N.; Goldsmith, B. R.; Janik, M. J. Sensitivity analysis of electrochemical double layer approximations on electrokinetic predictions: case study for CO reduction on copper. *J. Phys. Chem. C* **2024**, *128* (26), 10837−10847.
(59) Zhang, Z.; Bian, L.; Tian, H.; Liu, Y.; Bando, Y.; Yamauchi, Y.; Wang, Z.-L. Tailoring the surface and interface structures of copper-based catalysts for electrochemical reduction of CO_2 to ethylene and ethanol. *Small* **2022**, *18* (18), 2107450.
(60) Choi, H.; Lee, D.-K.; Han, M.-K.; Janani, G.; Surendran, S.; Kim, J. H.; Kim, J. K.; Cho, H.; Sim, U. Review non-noble metal-based single-atom catalysts for efficient electrochemical CO_2 reduction reaction. *J. Electrochem. Soc.* **2020**, *167* (16), 164503.

https://doi.org/10.1021/jacs.6c05085
J. Am. Chem. Soc. XXXX, XXX, XXX−XXX